

Autoionization dynamics of ($^2P_{1/2}$) ns/d states in krypton probed by noncollinear wave mixing with attosecond extreme ultraviolet and few-cycle near infrared pulses

Cite as: J. Chem. Phys. **151**, 114305 (2019); <https://doi.org/10.1063/1.5113912>

Submitted: 09 June 2019 • Accepted: 15 August 2019 • Published Online: 18 September 2019

 Ashley P. Fidler,  Hugo J. B. Marroux, Erika R. Warrick, et al.

COLLECTIONS

Paper published as part of the special topic on [Ultrafast Spectroscopy and Diffraction from XUV to X-ray](#)

 This paper was selected as an Editor's Pick



View Online



Export Citation



CrossMark

ARTICLES YOU MAY BE INTERESTED IN

[NaI revisited: Theoretical investigation of predissociation via ultrafast XUV transient absorption spectroscopy](#)

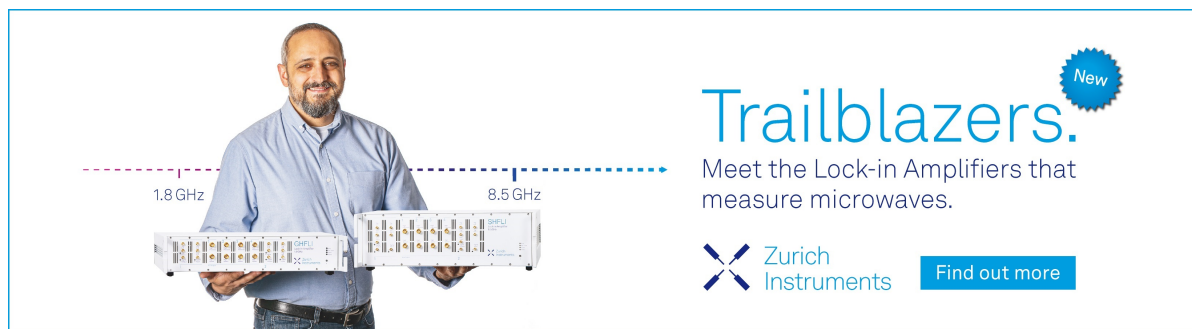
The Journal of Chemical Physics **151**, 204103 (2019); <https://doi.org/10.1063/1.5128105>

[XUV-beamline for attosecond transient absorption measurements featuring a broadband common beam-path time-delay unit and in situ reference spectrometer for high stability and sensitivity](#)

Review of Scientific Instruments **90**, 053108 (2019); <https://doi.org/10.1063/1.5091069>


[Communication: XUV transient absorption spectroscopy of iodomethane and iodobenzene photodissociation](#)

The Journal of Chemical Physics **145**, 011101 (2016); <https://doi.org/10.1063/1.4955212>



Trailblazers. New

Meet the Lock-in Amplifiers that measure microwaves.

 Zurich Instruments [Find out more](#)

Autoionization dynamics of ($^2P_{1/2}$) ns/d states in krypton probed by noncollinear wave mixing with attosecond extreme ultraviolet and few-cycle near infrared pulses

Cite as: J. Chem. Phys. 151, 114305 (2019); doi: 10.1063/1.5113912

Submitted: 9 June 2019 • Accepted: 15 August 2019 •

Published Online: 18 September 2019



View Online



Export Citation



CrossMark

Ashley P. Fidler,^{1,2}  Hugo J. B. Marroux,^{1,2}  Erika R. Warrick,^{1,2} Etienne Bloch,¹ Wei Cao,^{1,2} Stephen R. Leone,^{1,2,3}  and Daniel M. Neumark^{1,2,a)} 

AFFILIATIONS

¹Chemical Sciences Division, Lawrence Berkeley National Laboratory, Berkeley, California 94720, USA

²Department of Chemistry, University of California, Berkeley, California 94720, USA

³Department of Physics, University of California, Berkeley, California 94720, USA

Note: This paper is part of the JCP Special Collection on Ultrafast Spectroscopy and Diffraction from XUV to X-ray.

^{a)}E-mail: dneumark@berkeley.edu

ABSTRACT

The autoionization dynamics of the ($^2P_{1/2}$) ns/d Rydberg states in krypton are investigated using spatially isolated wave-mixing signals generated with a short train of subfemtosecond extreme ultraviolet (XUV) pulses and noncollinear, few-cycle near infrared pulses. Despite ubiquitous quantum beat oscillations from XUV-induced coherences within the excited-state manifold, these wave-mixing spectra allow for the simultaneous evaluation of autoionization lifetimes from a series of Rydberg states above the first ionization potential. Experimentally measured lifetimes of 22 ± 8 fs, 33 ± 6 fs, and 49 ± 6 fs for the wave-mixing signals emitting from the ($^2P_{1/2}$)6d/8s, ($^2P_{1/2}$)7d/9s, and ($^2P_{1/2}$)8d/10s resonances compare favorably with lifetimes for the ($^2P_{1/2}$)6d, 7d, and 8d Rydberg states determined from spectral linewidths. Analysis of the quantum beats reveals that the enhancement of wave-mixing pathways that couple the ($^2P_{1/2}$) nd states to themselves leads to individual reporter state-dependent decays in the wave-mixing signals. The results demonstrate the promise of wave-mixing spectroscopies with subfemtosecond XUV pulses to provide valuable insights into processes governed by electronic dynamics.

Published under license by AIP Publishing. <https://doi.org/10.1063/1.5113912>

I. INTRODUCTION

Dynamics governed by electronic processes occur on some of the shortest timescales in nature, ranging from hundreds of attoseconds ($1 \text{ as} = 10^{-18} \text{ s}$) to a few femtoseconds ($1 \text{ fs} = 10^{-15} \text{ s}$).^{1–3} Until recently, the lifetimes of these ultrafast processes typically have been determined through spectral lineshape measurements in the frequency domain. However, effects such as finite spectral resolution, heterogeneous and homogeneous broadening, and spectral congestion often prevent the retrieval of accurate lifetimes associated with the underlying electronic dynamics.⁴ With the advent of high harmonic generation (HHG)-based techniques to produce attosecond pulses in the extreme ultraviolet (XUV) and soft X-ray regimes, these

dynamics have become accessible to direct measurement in the time domain. Transient absorption and photoelectron techniques utilizing attosecond pulses have been developed and employed to measure dynamic processes including autoionization,^{4,5} Auger decay,⁶ and charge migration.⁷ However, the observed time-dependent spectra are often complicated by overlapping spectral effects, precluding quantitative measurements in complex systems. Here, nonlinear wave-mixing spectroscopy is utilized to investigate autoionization in krypton without the interference of many of these complicating effects.

Nonlinear spectroscopies are regularly employed in the optical, infrared, and radiofrequency regimes to probe complex systems with high selectivity.^{8,9} In these investigations, intense

electromagnetic fields coherently induce a macroscopic polarization in a target medium with significant contributions from higher-order terms, which can be expressed as

$$P = \epsilon_0(\chi^{(1)}E + \chi^{(2)}EE + \chi^{(3)}EEE + \dots), \quad (1)$$

where ϵ_0 is the vacuum permittivity, $\chi^{(n)}$ is the n th-order susceptibility, and E is the electric field. In an isotropic medium, these higher-order terms result in emission from nonlinear, or wave-mixing, processes dependent upon odd orders of $\chi^{(n)}$. Nonlinear techniques capitalize on the conservation of momentum and energy in the generation of the newly emitted field to resolve and measure signals that are often obscured in other techniques. Examples include measurements of energy transfer dynamics in light harvesting complexes with two-dimensional electronic spectroscopy,^{10–12} studies probing the properties of surfaces and interfaces with second harmonic generation (SHG)-based methods,^{13,14} and imaging in biological samples with coherent anti-Stokes Raman microscopy.^{15,16}

In our laboratory, we have developed a nonlinear XUV spectroscopy utilizing attosecond XUV pulses produced by HHG and two few-cycle near infrared (NIR) pulses to probe electronic dynamics in atoms and small molecules. The implementation of a noncollinear beam geometry between the three pulses has proven particularly powerful, as it facilitates the spatial separation of desired wave-mixing signals through phase-matching. These experiments have successfully measured both electronic and vibrational wave packet dynamics,^{17–21} characterized the outer well of a previously inaccessible dark state in N_2 ,²⁰ and produced the first experimental demonstration of two dimensional spectroscopy in the XUV.²¹ In a recent study, the nonperturbative nature of noncollinear wave-mixing with these ultrashort, intense pulses was explored in He, revealing that the accumulation of the AC Stark phase over the NIR pulse duration leads to delays in higher-order signal generation.²² However, all of these experiments were performed on systems containing only long-lived Rydberg states, and the generation and time dependence of nonlinear signals from XUV-excited states that decay on ultrafast timescales have yet to be established.

In this work, multiple orders of spatially isolated wave-mixing signals from bound and autoionizing states are generated in krypton using a noncollinear geometry between a short train of sub-femtosecond XUV pulses and two time-coincident few-cycle NIR pulses. The resulting wave-mixing spectra probe the autoionization dynamics of an extended manifold of Rydberg states simultaneously. Pronounced quantum beating provides detailed information about the evolving XUV-induced coherence and NIR-mediated coupling of Rydberg states. Despite extensive coupling within the manifold of states, lifetimes of individual $4s^24p^5(^2P_{1/2})nd$ autoionizing states can be retrieved directly in the time domain, yielding values very close to those calculated from frequency-domain linewidth measurements. Fourier analysis reveals dominant contributions from wave-mixing pathways that preferentially couple the $(^2P_{1/2})nd$ autoionizing states with themselves, leading to the observed reporter-state specific decays. While the mechanism is still unknown, the relative enhancement of these pathways does not appear to arise from a purely perturbative picture of wave-mixing, suggesting that non-perturbative effects may impact nonlinear signal evolution in this system. These results demonstrate that wave-mixing spectroscopies

constitute a powerful method for the study of ultrafast dynamics in the XUV regime, providing an alternative to spectrally complex transient absorption measurements.

II. EXPERIMENTAL METHODS

The apparatus utilized for background-free attosecond wave-mixing measurements has been described previously^{20,22} and is shown in Fig. 1(a). A 2 mJ/pulse, 1 kHz repetition rate Ti:sapphire commercial femtosecond laser system (Femtopower HE, Femtolasers) produces 22 fs NIR pulses at a central wavelength of 760 nm. The output spectrum is spectrally broadened in a 400 μ m inner diameter hollow core fiber filled with 1.2 bar of neon gas and is subsequently recompressed in time by six pairs of broadband chirped mirrors (Ultrafast Innovations) and a 1 mm thick ammonium dihydrogen phosphate (ADP) plate,²³ resulting in 6 fs pulses that span a wavelength ranging from 550 to 950 nm. A 50:50 beam splitter divides the broadband light into two arms. The light transmitted through the beam splitter is focused by a 50 cm focal length mirror into a vacuum chamber at 10^{-3} Pa (10^{-6} Torr) that contains a cell statically filled with xenon gas for high harmonic generation. The interaction of the few-cycle NIR pulse with the gas generates a pulse train consisting of 2–3 subfemtosecond XUV pulses. A 0.1 μ m In foil (Lebow) attenuates the driving NIR beam and selects harmonics between 11 and 17 eV, allowing the XUV to access states both below and above the first ionization potential (IP) of Kr at 14.0 eV. A gold-coated toroidal mirror focuses the XUV through an annular mirror into a 1 mm path length (diameter) sample cell containing 1467 Pa (11 Torr) of krypton gas. Holes approximately 500 μ m in diameter drilled through both sides of the HHG and sample cells allow for the passage of light and continuous escape of the used gas. The XUV intensity is estimated to be 10^8 – 10^{10} W cm⁻² in the target cell due to the low conversion efficiency of HHG.

The intensity necessary to support nonlinear processes is provided by the NIR light reflected by the 50:50 beam splitter. These few-cycle NIR pulses are delayed relative to the XUV with a piezoelectric stage [P-622 with E509 controller, Physik Instrumente (PI)] and then split into two separate arms by a 50:50 beam splitter. Two 1 m focal length mirrors direct the reflected and transmitted arms vertically above and below the hole of the annular mirror in the vacuum chamber before achieving beam diameters of ~ 100 μ m (FWHM) and a combined intensity of 2×10^{12} W cm⁻² in the target cell. To ensure spatial separation of signals originating from multiphoton wave-mixing pathways from the harmonics, the two NIR beams intersect the XUV in a noncollinear geometry at angles of approximately 18 mrad (1°) and 13 mrad (0.75°) for the upper and lower arms, respectively [Fig. 1(b)]. In the experiments described here, the two NIR pulses are time-coincident. A second piezoelectric stage is placed in the arm transmitted through the 50:50 beam splitter to compensate for daily fluctuations in the length of the two arms. Temporal and spatial overlap between the XUV and both NIR arms is determined by removing the metallic foil blocking the copropagating NIR after HHG and inserting a removable mirror into the beam path after the annular mirror, directing all three NIR beams outside the vacuum apparatus to an optical CMOS camera (DCC1545M, Thorlabs). The positions of the stages are modified manually until interference fringes are observed between all beams (see [supplementary material](#), Fig. 1). The crossing angle θ_{crossing} can be

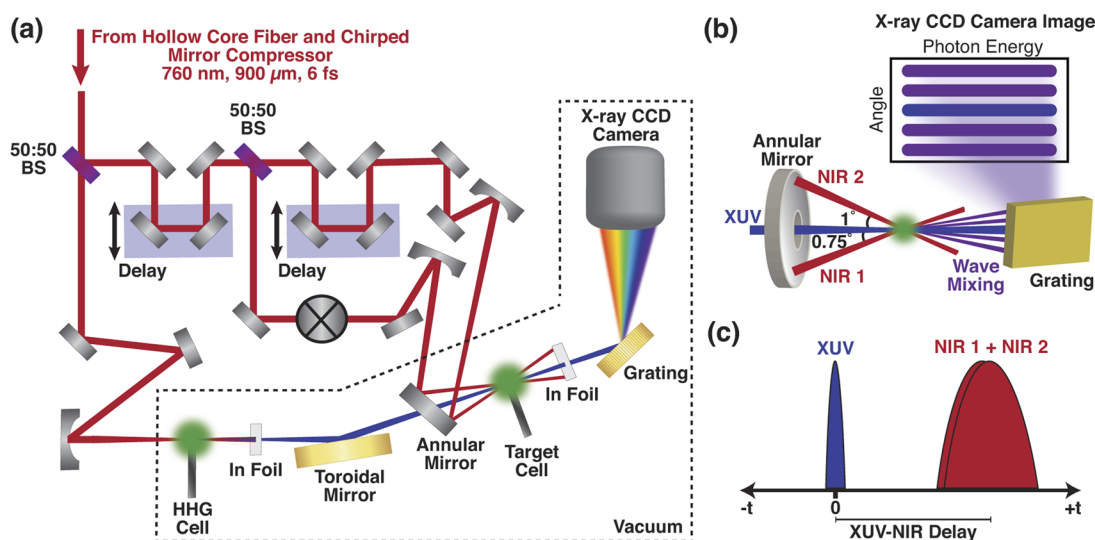


FIG. 1. Experimental apparatus and pulse sequence. (a) Experimental apparatus after NIR pulse compression used for noncollinear wave-mixing experiments. (b) The interaction of the noncollinear NIR pulses with the XUV-excited sample leads to spatial separation of wave-mixing signals. The NIR beam oriented below the hole mirror is labeled NIR 1, while the beam oriented above the mirror is labeled NIR 2. (c) Dynamics encoded in wave-mixing signals are measured as a function of the time delay between the XUV and time-coincident NIR pulses. Positive delays indicate that the XUV pulse precedes the NIR pulses.

calculated from the fringe spacing via the following equation:

$$\theta_{\text{crossing}} = 2 \sin^{-1}(\lambda_{\text{NIR}}/2x), \quad (2)$$

where λ_{NIR} is the central NIR wavelength and x is the fringe spacing.

A 0.15 μm In foil (Lebow) attenuates the NIR beams after the sample cell. The transmitted XUV light is dispersed in frequency by a gold-coated flat-field grating (01-0464, Hitachi) and recorded as a function of both frequency and phase-matching divergence angle by a 1340 × 400 pixel X-ray CCD camera (Pixis XO 400B, Princeton Instruments). From the absorption features of long-lived Rydberg states in argon, the spectral resolution at 14.3 eV is expected to be 19 meV. The signal from a total of 1500 laser pulses is accumulated at each XUV-NIR delay. Here, positive delays indicate that the XUV pulse precedes the time coincident NIR pulses [Fig. 1(c)]. A step size of 300 was chosen to resolve short-lived features around time overlap. To examine longer-lived features, the step size was increased to 1 fs and 3 fs at XUV-NIR delays of 130 fs and 312 fs, respectively. The energy axis of the CCD camera was calibrated daily using atomic transition line data available from the National Institute of Standards and Technology (NIST) for the Rydberg states of argon. Except where noted, the data are presented in terms of absorbance

$$A = -\log_{10}(I/I_0), \quad (3)$$

where I is the light transmitted through the krypton sample at a given XUV-NIR delay and I_0 is a reference spectrum taken without krypton gas in the sample cell before each delay-dependent scan. Absorption features have positive absorbance values, while emission features from wave-mixing processes have negative absorbance values. For wave-mixing signals spatially isolated from the incident

XUV pulse, I_0 comprises the dark counts from the CCD plus any residual scattered light from the XUV and NIR arms. This signal presentation mode is chosen to emphasize the weaker wave-mixing signals and indicate that they originate explicitly from newly generated light.

III. RESULTS

A. Spatial isolation of resonance-enhanced wave-mixing emission signals

A noncollinear geometry between a short XUV pulse train and two few-cycle NIR pulses results in background-free wave-mixing signals in krypton from the $4s^2 4p^5(^2P_{1/2})nl$ states above the first IP (14.0 eV). These states can autoionize to form the $\text{Kr}^+ 2P_{3/2}$ state. To generate wave-mixing signals that probe these autoionizing states, the broadband XUV pulse train (13.5–16.0 eV) induces a coherent superposition between the ground state and a manifold of bound and autoionizing states that decays with the dephasing time (polarization lifetime) of the constituent states.²⁴ The addition of two moderately intense, noncollinear NIR pulses produces wave-mixing signals that emit at a wavevector dependent upon the sum of the initial XUV (k_{XUV}) and NIR (k_{NIR1} and k_{NIR2}) wavevectors.

An X-ray CCD camera image taken at temporal overlap of all three pulses is shown in Fig. 2(a). The image comprises several bands, each of which results from one or more phase-matching conditions illustrated in Fig. 2(b). The spatial dimension of the image is reported in divergence angle relative to the incident XUV beam. For each photon of the wave-mixing pathway resonant with an electronic transition in the atom, the intensity of the emitted signal is enhanced. All one-photon dipole-forbidden np (dark) states

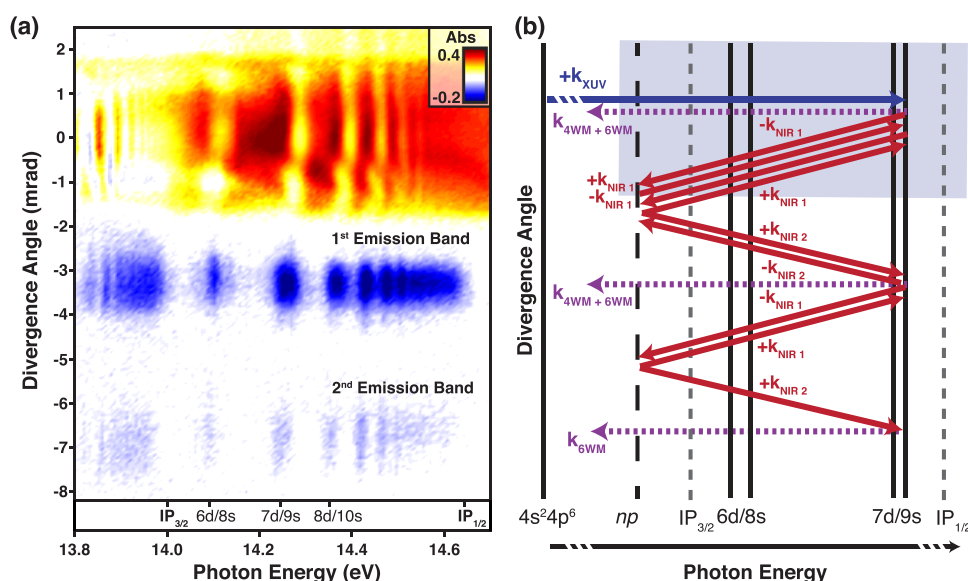


FIG. 2. Spatially dependent emission of multiple orders of wave-mixing signals. (a) An X-ray charge coupled device (CCD) image plotted as a function of photon energy and phase-matching divergence angle exhibits three distinct bands of absorption or wave-mixing signals. The energies of the first two ionization potentials and several key autoionizing states are provided at the bottom of the image. (b) Example phase-matching diagrams show wave-mixing pathways that emit at each of the three bands at the $(^2P_{1/2})7d/9s$ resonance at 14.26 eV. The two bands closest to 0 mrad contain contributions from multiple orders of wave-mixing signals. The blue and red solid arrows indicate XUV and NIR photons, respectively. The dotted purple arrows indicate photons of generated XUV wave-mixing light.

accessible by one NIR photon from the ns/d autoionizing states are located below the first IP.

In the band centered at 0 mrad, positive absorbance values indicate the linear absorption of high harmonic XUV light by atomic resonances both above and below the first IP. At time overlap, the XUV-induced polarization is perturbed by the NIR pulses, leading to a variety of spectral effects, including spectral broadening and modification of absorption lineshapes shifting of atomic resonances, and depletion of features.^{2,4,25,26} As shown by the phase-matching diagrams in Fig. 2(b), the spectrum at 0 mrad will also exhibit contributions from multiphoton wave-mixing pathways that terminate without an overall change of the emission angle such that

$k_{XUV} - k_{NIR1} + k_{NIR1} \approx k_{XUV}$. The delay-dependence of these features is discussed in Sec. III C.

A distinct band of strong negative absorbance (emission) features is observed below the harmonic axis from -2.5 to -4.3 mrad at the bright state energies. These features originate from wave-mixing pathways that employ photons from both NIR arms (NIR 1 and NIR 2). As shown in Fig. 2(b), both four-wave mixing ($k_{4WM} = k_{XUV} - k_{NIR1} + k_{NIR2}$) and six-wave mixing ($k_{6WM} = k_{XUV} - k_{NIR1} + k_{NIR2} - k_{NIR1} + k_{NIR1}$) processes can contribute to this band. For four-wave mixing processes dependent on both NIR pulses, wave-mixing signals emit at divergence angles, ϕ_{div} , approximately equal to the following expression:

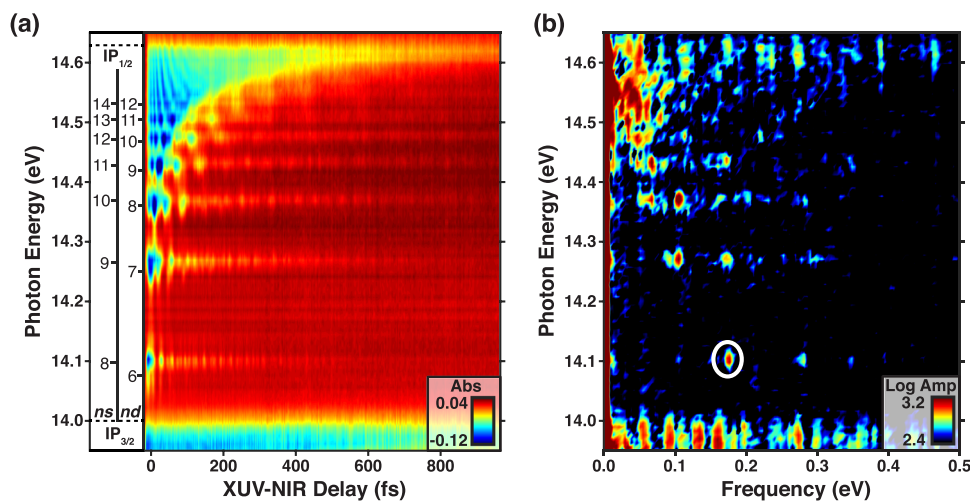


FIG. 3. Wave-mixing measurements of $(^2P_{1/2})nl$ autoionizing states of Kr. (a) Wave-mixing spectrum of the signals in the first emission band as a function of energy and XUV-NIR delay. State assignments are provided to the left of the panel. (b) Fourier analysis of the delay-dependent spectrum. The white circle highlights a feature arising from the interference of two wave-mixing pathways that is discussed explicitly in Fig. 8.

$$\phi_{\text{div}} \approx \frac{v_{\text{NIR1}}\theta_{\text{NIR1}} + v_{\text{NIR2}}\theta_{\text{NIR2}}}{v_{\text{XUV}}}, \quad (4)$$

where v_{NIR1} and v_{NIR2} are the frequencies of the two relevant NIR interactions and v_{XUV} is the frequency of the initial XUV absorption. For example, as shown in Fig. 2(b), one of the wave-mixing pathways that gives rise to the signal at 14.26 eV involves one XUV photon from the ground state to the ($^2\text{P}_{1/2}$)9s bright state (14.26 eV) and two NIR photons resonant with the ($^2\text{P}_{1/2}$)6p dark state (1.5 eV). Using the measured NIR crossing angles of 18 and 13 mrad and Eq. (4), this pathway emits at a divergence angle of -3.3 mrad, which is consistent with the experimentally observed central divergence angle of -3.4 mrad. Discrepancies between observed and calculated emission angles can be attributed to error in the measured crossing angles and the presence of multiple different wave-mixing pathways that emit at slightly different angles. In the transient grating picture of wave-mixing, these signals are described as the first diffraction order.^{27,28} For simplicity, we refer to these features between -2.5 and -4.3 mrad as the first emission band.

A weaker band of wave-mixing signals can be observed between -6.1 and -7.8 mrad. As shown in Fig. 2(b), these features primarily correspond to six-wave mixing processes that employ one XUV photon and two photons from each NIR pulse ($k_{\text{6WM}} = k_{\text{XUV}} - k_{\text{NIR1}} + k_{\text{NIR2}} - k_{\text{NIR1}} + k_{\text{NIR2}}$). The divergence angle expected for these processes can be calculated using a relationship similar to Eq. (4),

$$\phi_{\text{div}} \approx \frac{2(v_{\text{NIR1}}\theta_{\text{NIR1}} + v_{\text{NIR2}}\theta_{\text{NIR2}})}{v_{\text{XUV}}}. \quad (5)$$

For a five photon process involving one 14.26 eV photon and four 1.5 eV photons, the calculated divergence angle is -6.6 mrad. The six-wave mixing features at these divergence angles comprise the second emission band.

B. Delay-dependent wave-mixing emission from autoionizing states in krypton

The temporal profile of the bound and autoionizing states probed can be accessed by integrating over the angular range of the first emission band on the CCD camera image [Fig. 2(a)]. Plotting the result as a function of the delay between the XUV pulse train and the two time-coincident NIR pulses reveals information about the evolution of the XUV-induced coherence. Figure 3(a) shows a false color plot of the wave-mixing signal as a function of photon energy and XUV-NIR delay. Wave-mixing signals appear as negative absorbance (emission) features at the energies of atomic resonances. High-resolution photoabsorption linewidth measurements previously determined the lifetimes of the first *d*- and *s*-character states above the IP, ($^2\text{P}_{1/2}$)6d and ($^2\text{P}_{1/2}$)8s, to be 23.5 fs and 949.5 fs, respectively, indicating that the *d*-character states are better coupled to the underlying continuum.²⁹ Due to a larger quantum defect for the *s*-character Rydberg series, *nd* and *n's* states, where $n' = n + 2$, possess similar effective principal quantum numbers, n^* , and appear close in energy.^{30,31} As expected from examining the overlap integral, the lifetimes of autoionizing states lengthen with n^* and therefore with increasing energy. The spectral resolution is insufficient to fully resolve individual wave-mixing signals emitting from adjacent *nd/n's* states as well as from the finely spaced states approaching the IPs.

Just below the first IP at 14.0 eV, wave-mixing features emitting from the bound states do not decay appreciably within the time frame of the experiment. In contrast, wave-mixing signals emitting from the spectrally overlapped long-lived *n's* and short-lived *nd* autoionizing states above the IP exhibit visible decays. At each resonance, an intense, relatively short-lived feature can be distinguished from weaker, longer-lived quantum beat oscillations that persist for the entirety of the experiment. This short-lived feature is approximately five times more intense than the longer-lived component. Notably, the duration of the shorter-lived component increases with $(n^*)^3$ of the emission state, following the known trend for autoionizing state lifetimes. The quantum beat oscillations that underlie both

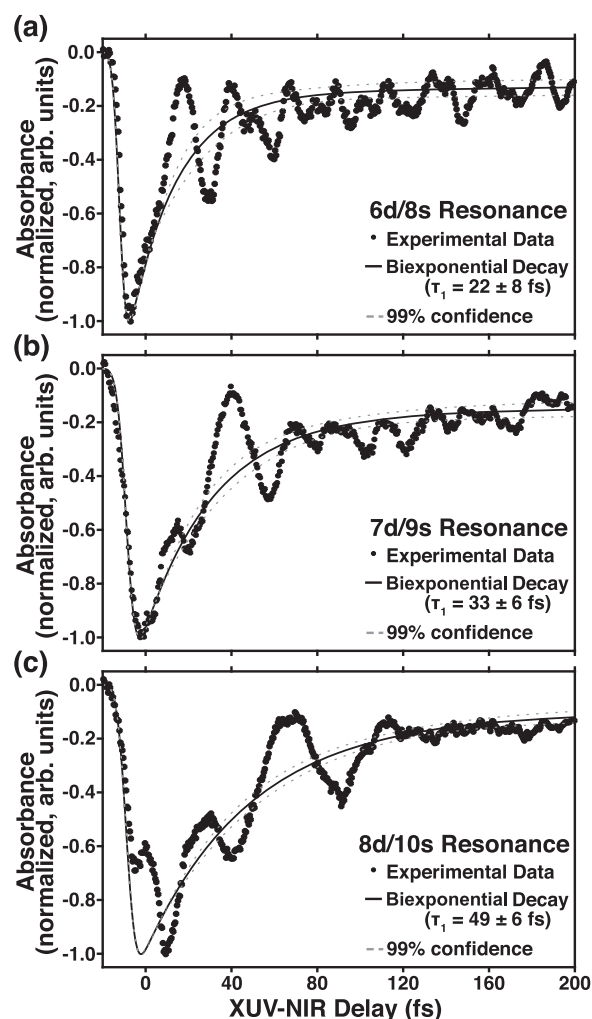


FIG. 4. Lifetime analysis of ultrafast wave-mixing decays. Lineouts taken from the delay-dependent first emission band of wave-mixing signals at the (a) ($^2\text{P}_{1/2}$)6d/8s resonance (14.1 eV), (b) ($^2\text{P}_{1/2}$)7d/9s resonance (14.26 eV), and (c) ($^2\text{P}_{1/2}$)8d/10s resonance (14.37 eV) are fit to biexponential decays with an arbitrary long time constant. The fit short time constant compares favorably with the excited state population lifetimes known for the ($^2\text{P}_{1/2}$)6d, ($^2\text{P}_{1/2}$)7d, and ($^2\text{P}_{1/2}$)8d states, respectively (see text for details).

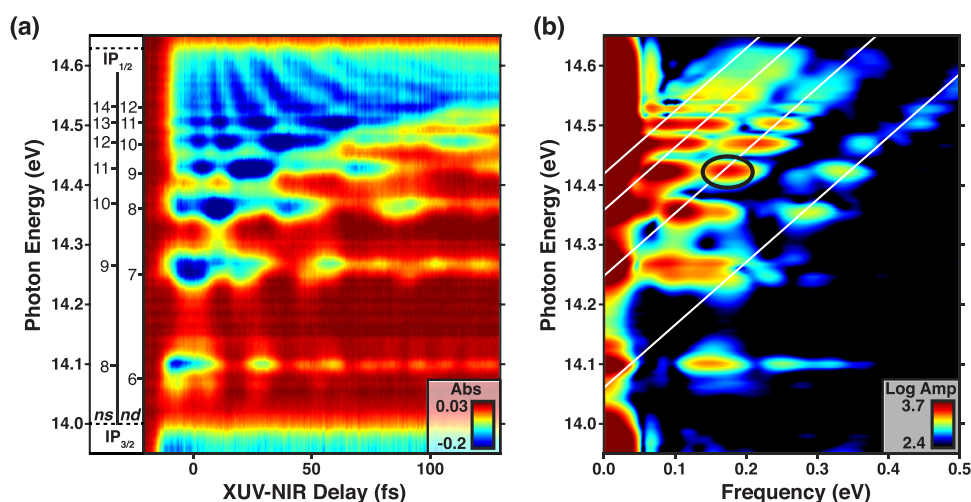


FIG. 5. Early delay-dependence of wave-mixing signals in Kr. (a) Delay-dependent spectrum of the signals in the first emission band windowed to encompass only XUV-NIR delays from -20 to 130 fs. State assignments are provided to the left of the panel. (b) Fourier analysis of the windowed delay-dependent spectrum. The white lines have unity slope and indicate that the features along them arise in part from a wave-mixing pathway that begins with the absorption of an XUV photon to generate the state at the intercept. The feature highlighted by the black circle is identified in Fig. 8(b).

the short and long time components in the time-domain spectrum arise from the interference of wave-mixing pathways, as described in more detail below. Constituent pathways can be identified from the oscillation frequencies as determined by a Fourier transform along the delay axis [Fig. 3(b)]. Strong, distinct features appear at 0.067 eV, 0.105 eV, 0.176 eV, and 0.28 eV in the lower-lying states.

To assess the short-lived time component, three wave-mixing features at the energies of 14.1 eV, 14.26 eV, and 14.37 eV are fit to a convolution of the instrumental response and a biexponential decay using a Levenberg–Marquardt least squares algorithm (Fig. 4). Given that the long-lived quantum beats endure well over an order of magnitude longer than the short-lived features, the long-time component was fixed at an arbitrarily long value. Varying the value of the long time constant between 500 fs and 1 ns did not significantly alter the value of the short-time constant. This fitting procedure yields decays of 22 ± 8 fs, 33 ± 6 fs, and 49 ± 6 fs for the short-lived components of the features emitting from the $(^2P_{1/2})6d/8s$,

$(^2P_{1/2})7d/9s$, and $(^2P_{1/2})8d/10s$ states, respectively, verifying the qualitative observation that the duration of the short-lived component increases proportionally with $(n^*)^3$ of the d -character reporter state.

Windowing the wave-mixing spectrum to include only the first 130 fs after time overlap emphasizes the dynamics of the short-lived component [Fig. 5(a)]. In the dense band of emission approaching the second ionization potential at 14.63 eV, the frequency of the dominant quantum beat increases with energy, creating hyperbolic band structures. As shown in Fig. 5(b), the Fourier transform of just these early delays (-20 fs to 130 fs) is visibly distinct from the transform that encompasses longer delays [Fig. 3(b)]. The origin of these differences is covered in Sec. IV A. The majority of features in Fig. 5(b) fall on lines with unity slope and an intercept at the energy of one of the lower lying $(^2P_{1/2})nd$ states. As in the full transform, these features must originate from the interference of two multiphoton pathways in the wave-mixing spectrum.

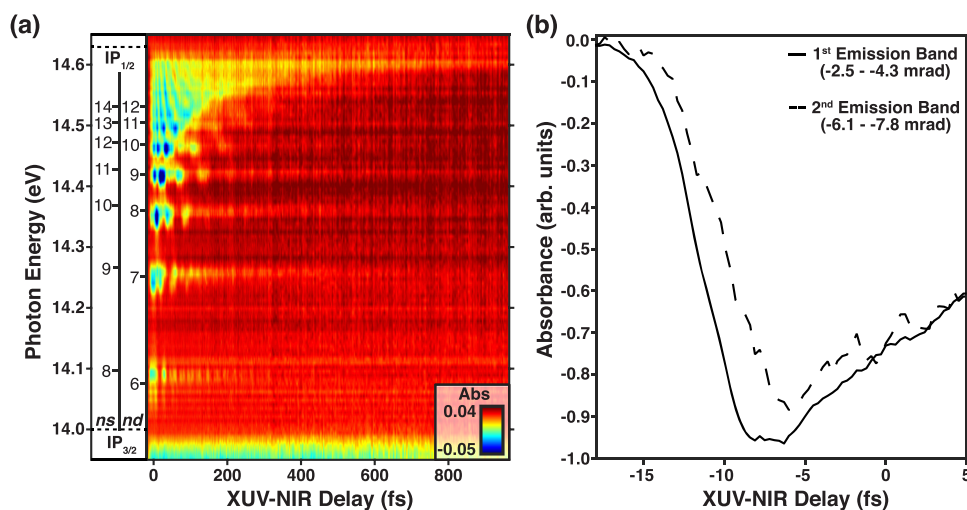


FIG. 6. Six-wave mixing measurements of autoionizing states of Kr. (a) Wave-mixing spectrum of the six-wave mixing signals in the second emission band as a function of energy and XUV-NIR delay. State assignments are provided to the left of the panel. (b) Lineouts of wave-mixing signals generated at the $(^2P_{1/2})6d/8s$ resonance (14.1 eV) obtained by integrating over the first emission band (-2.5 to -4.5 mrad) or the second emission band (-6.1 to -7.8 mrad) in the CCD camera image shown in Fig. 2(a).

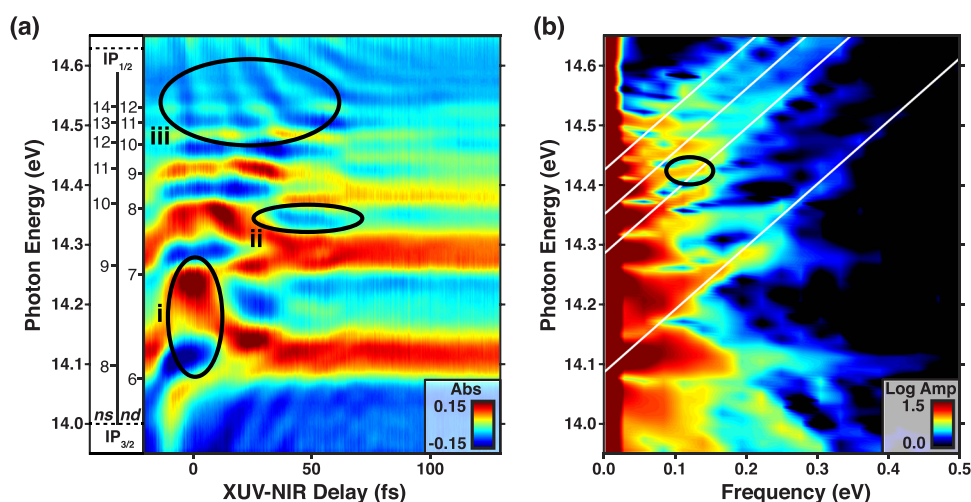


FIG. 7. Transient absorption measurements of autoionizing states of Kr. (a) Absorption is plotted as a function of XUV-NIR delay and energy. States assignments are located to the left of the panel. Black ellipses indicate features of interest discussed in the text. (b) Fourier analysis of the delay-dependent spectrum. The white lines possess a unity slope and indicate that the features along them arise from the interference of the linear response and a wave-mixing pathway that begins with the absorption of an XUV photon to generate the state at the intercept. The feature circled in black is discussed further in Fig. 8(a).

Six-wave mixing signals are captured by integrating over the second emission band between -6.1 and -7.8 mrad on the CCD camera image in Fig. 2(a). A false color plot demonstrating the evolution of the emission as a function of photon energy and XUV-NIR delay is shown in Fig. 6(a). Although the signal-to-noise ratio is lower, the isolated six-wave mixing features exhibit dynamics equivalent to those observed in the previously described first emission band with four- and six-wave mixing contributions. However, the second emission band emerges at later XUV-NIR delays than the first emission band. As shown in Fig. 6(b), the six-wave mixing signal emitting from the $(^2P_{1/2})6d/8s$ autoionizing state in the second emission band is delayed by 1.8 ± 0.4 fs relative to the corresponding wave-mixing signal in the first emission band. A similar delay was seen in He²² and is discussed further in Sec. IV B.

C. Comparison to transient absorption of autoionizing states in krypton

Integrating over the absorption band situated between 2 and -1.2 mrad on the CCD camera image yields an attosecond transient absorption measurement of the autoionizing state dynamics of Kr [Fig. 7(a)]. Here, positive (absorption) features arise at the energies of the autoionizing states. Substantial energy shifts of the resonances around pulse overlap and adjacent bands at later delays indicated in ellipses (i) and (ii) can be attributed to the AC Stark effect, which gives rise to a laser-imposed phase shift that accumulates over the NIR pulse duration.^{22,25,26,32,33} In addition to the AC Stark effects, evidence of wave-mixing processes can be observed at early delays through quantum beat oscillations highlighted in ellipse (iii) and described in detail in previous publications.²⁵ As in the wave-mixing spectra, the quantum beats approaching the second IP increase in frequency with photon energy, creating hyperbolic band structures. The most prominent features in the corresponding Fourier transform appear along lines of unity slope that intercept the y-axis at the energies of bright state resonances [Fig. 7(b)]. The delay dependence extending to nearly 1 ps and the corresponding Fourier transform are provided in the [supplementary material](#), Fig. 2.

IV. DISCUSSION

A. Explanation of experimentally observed wave-mixing signals

The results of these noncollinear wave-mixing experiments with subfemtosecond XUV and few-cycle NIR pulses conclusively indicate that nonlinear XUV spectroscopies can access ultrafast decays of electronic excited states with notable advantages over transient absorption. From the CCD camera image alone [Fig. 2(a)], it is clear that the pulses employed in these experiments supply sufficient intensity to induce wave-mixing from the $4s^24p^5(^2P_{3/2})nl$ and $(^2P_{1/2})nl$ states of Kr, which exhibit a larger range of photoabsorption cross sections and decay rates than previously studied systems. Particularly notable is the observation of spatially isolated wave-mixing signals at the energies of the spectrally broad XUV-generated autoionizing states above the first IP. The time and frequency-domain spectra of these emission signals reveal a global view of autoionization dynamics occurring above the first IP in this system [Fig. 3(a)].

Despite substantial quantum beat oscillations indicative of contributions from multiple different states to each emission signal, the duration of the intense, short-lived component of the wave-mixing features increases with $(n^*)^3$ of the reporter (emitting) state, following the trend expected for the Rydberg state lifetimes. As shown in Table I, the experimentally measured decay constants for the

TABLE I. Comparison of measured wave-mixing lifetimes with literature values. Lifetimes measured in the time-domain for three wave-mixing signals in the first emission band compare favorably with lifetimes of the $(^2P_{1/2})nd$ reporter states determined from linewidth measurements.

Reporter state	Wave-mixing lifetime (fs)	Literature lifetime (fs) ²⁹
$(^2P_{1/2})6d$	22 ± 8	23.5
$(^2P_{1/2})7d$	33 ± 6	34.0
$(^2P_{1/2})8d$	49 ± 6	47.1

short-lived components of the ($^2P_{1/2}$)8s/6d, 9s/7d, and 10s/8d wave-mixing features agree favorably with the population lifetimes of the ($^2P_{1/2}$)6d, 7d, and 8d Rydberg states.²⁹ While more disruptive quantum beat oscillations preclude quantitative fits of higher photon energy features, the lifetimes retrieved for these lower energy emission signals suggest that the short-lived time component can be attributed to wave-mixing pathways probing the ($^2P_{1/2}$)*nd* autoionizing states. The relationship between the measured wave-mixing emission lifetime and that of the ($^2P_{1/2}$)*nd* reporter state is noteworthy as it indicates that a single wave-mixing pathway dominates over other pathways that also contribute to the emission signal.

Fourier analysis of the wave-mixing emission signals can provide insight into the wave-mixing pathways that contribute to the delay dependence of the emitted signals. The Fourier transform of the time-domain data including XUV-NIR delays up to 965 fs largely provides evidence of coherences from the long-lived *ns* autoionizing states with lifetimes on the scale of picoseconds [Fig. 3(b)]. For example, the prominent 0.176 eV frequency peak obtained from the ($^2P_{1/2}$)8s emission signal at 14.10 eV [circled in Fig. 3(b)] can be assigned to an XUV-induced coherence of the 8s (14.10 eV) and 9s (14.27 eV) autoionizing states. The XUV-induced coherence of these two states is coupled by two NIR photons to the ($^2P_{1/2}$)8s reporter state via a dark state of *p*- or *f*-electronic character [Fig. 8(a)]. The broad bandwidth of both the XUV and NIR pulses allows not only for the XUV-induced coherence of a manifold of excited states but also for extensive dark-state mediated coupling of states within the ~ 0.5 eV NIR bandwidth. Other prominent Fourier peaks at low photon energies can be assigned to the XUV-induced coherence of the 10s and 11s states (0.067 eV), 9s and 10s states (0.105 eV), and 8s and 10s states (0.28 eV). These features demonstrate the extensive coupling between Rydberg states that occurs within this system,

emphasizing that the observed wave-mixing signals probe the evolution of multiple XUV-excited states.

Fourier analysis of only early delays (~ 130 fs) reveals contributions from the shorter-lived *nd* autoionizing states [Fig. 5(b)]. The hyperbolic band structures in Fig. 5(a) generate peaks in the photon-energy resolved Fourier transform that fall on lines with unity slope, which are highlighted by white lines in Fig. 5(b). All features along the white lines arise from wave-mixing pathways that couple the state at the intercept with the final state at which the feature is observed. Here, the lines intercept the *y*-axis at the energies of the *nd* states preferentially. To produce such lines, the second interfering pathway is best described by a wave-mixing process with two degenerate NIR photons that couples the reporter state with itself. An example of two interfering pathways that lead to a peak in the early-delay Fourier transform is provided as pathways 1 and 2 in Fig. 8(b). Pathways with two degenerate NIR photons like pathway 2 appear to dominate the total emitted signal from the manifold of autoionizing states at early times, leading to the hyperbolic band structures and the intense, short-lived component observed in the time-domain wave-mixing signals, as discussed further in Sec. IV B.

Moreover, because of large contributions from these NIR-degenerate pathways, the delay-dependent wave-mixing spectrum provides more insight into the underlying excited state dynamics than a traditional transient absorption measurement. In previous attosecond transient absorption studies, AC-Stark effects were shown to limit the accuracy of lifetime measurements to only lineouts taken exactly on-resonance.⁴ As shown in Fig. 7(a), the severity of the AC Stark shift of the resonances around pulse overlap precludes any lineout measurement of the excited state lifetime, particularly of the short-lived ($^2P_{1/2}$)*nd* states. Without resolvable decays, the disappearance of quantum beat oscillations provides the

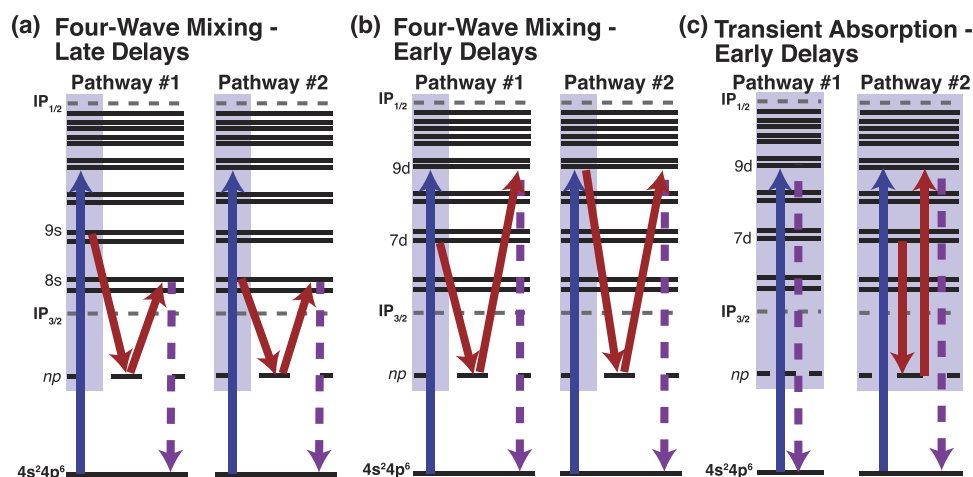


FIG. 8. Pathway interference leads to distinct quantum beat oscillations in wave-mixing and transient absorption measurements. Energy level diagrams showing two pathways that interfere to generate the observed signals at (a) late delays in the first emission band spectrum [white circle, Fig. 3(b)], (b) early delays in the first emission band spectrum [black circle, Fig. 5(b)], and (c) early delays in the transient absorption spectrum [black circle, Fig. 7(b)]. The assignment of relevant states is to the left of each pair of energy level diagrams. The blue and red solid arrows indicate XUV and NIR photons, respectively. The dotted purple arrows indicate photons of generated XUV wave-mixing light. The blue box illustrates the bandwidth of the XUV pulse.

most convincing evidence of autoionization in the transient absorption spectrum. The quantum beats produce peaks that appear along unity slope lines in the Fourier transform reminiscent of the features observed in the transform of the noncollinear wave-mixing signals at early delays [Fig. 7(b)]. These lines are interpreted as the interference of a one-photon, linear absorption pathway [Fig. 8(c), pathway 1] and a three-photon, wave-mixing pathway [Fig. 8(c), pathway 2] that emit at the state in which the beat occurs. The interference of one and three photon pathways is discussed extensively in the transient absorption literature.²⁵

B. General characteristics of wave mixing with ultrashort pulses

The conspicuous differences between transient absorption and wave-mixing spectra can be attributed to the presence or absence of the XUV field produced by HHG. In transient absorption experiments, NIR-induced features, including those generated by the AC Stark effect and wave-mixing pathways, interfere with the incident high harmonic XUV light. The XUV field thus acts as a reference field, allowing for phase-sensitive heterodyne detection.⁹ Using a square law detector, the intensity of the detected signal can be described by the following relationship:

$$I_{\text{signal}} = |E_{\text{XUV}} + E_{\text{emit}}|^2 = |E_{\text{XUV}}|^2 + |E_{\text{emit}}|^2 + 2\Re(E_{\text{emit}}E_{\text{XUV}}^*), \quad (6)$$

where I_{signal} is the intensity of the detected signal, E_{XUV} is the electric field of the incident XUV pulse train, and E_{emit} is the electric field of generated polarization signal. When the incident XUV field is present, E_{emit} includes both the first order polarization and any higher-order polarization fields. In a perturbative picture, the intensity of the incident XUV field can be assumed to be greater than the generated light. The intensity detected by the CCD camera can then be described by the following expression:

$$I_{\text{signal}} = |E_{\text{XUV}} + E_{\text{emit}}|^2 \approx |E_{\text{XUV}}|^2 + 2\Re(E_{\text{emit}}E_{\text{XUV}}^*). \quad (7)$$

The time-domain dynamics of the detected field in this self-heterodyned detection scheme are dominated by the cross term.⁹

For wave-mixing measurements in a noncollinear geometry, the reference XUV field does not overlap spatially with generated wave-mixing signals, resulting in a homodyne detection scheme. In optical homodyne detection, the square modulus of the incident field and the cross term can be ignored. The detected intensity can therefore be adequately described by only the square modulus of the emitted field, which only includes wave-mixing fields and, for a four-wave mixing process, is proportional to the polarization response function, $R^{(3)}(t_3, t_2, t_1)$,

$$|E_{\text{emit}}|^2 = |E_{\text{WM}}|^2 \propto |R^{(3)}(t_3, t_2, t_1)|^2, \quad (8)$$

where E_{WM} is the electric field of the wave-mixing signals. The time convention for t_1 , t_2 , and t_3 is defined in Fig. 9(a). The relevant components of the wave mixing response function for a single, arbitrary four-wave mixing pathway [Fig. 9(b)] utilized in our experiment can be defined as

$$R^{(3)}(t_3, t_2, t_1) \propto \mu_{01}^2 \mu_{12}^2 e^{-i(\omega_1 - \omega_0)t_1 - t_1/T_2}, \quad (9)$$

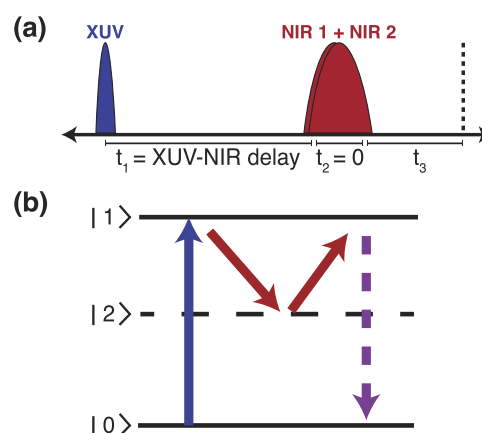


FIG. 9. Pulse sequence and generalized four-wave mixing pathway. (a) The pulse sequence utilized in this experiment. (b) A nonspecific wave-mixing pathway with two degenerate NIR photons. The blue and red solid arrows indicate XUV and NIR photons, respectively. The dotted purple arrows indicate photons of generated XUV wave-mixing light. See the [supplementary material](#), Note 3, for more information.

where μ_{01} and μ_{12} are the transition dipoles associated with the transition between states $|0\rangle$ and $|1\rangle$ and between states $|1\rangle$ and $|2\rangle$. The frequencies of states $|0\rangle$ and $|1\rangle$ are described by ω_0 and ω_1 , respectively. The decay term T_2 describes the dephasing time, which equals twice the population lifetime (T_1) for a system in which dephasing due to the environment is negligible.⁹ A more detailed derivation of the third-order response function using diagrammatic perturbation theory is provided in the [supplementary material](#), Note 3. In heterodyne detection schemes dominated by the cross term, the observed decay is equal to T_2 . To demonstrate the impact of this homodyne detection scheme on a time-domain signal, the response function is incorporated into Eq. (8) as follows:

$$|E_{\text{WM}}|^2 \propto \left| \mu_{01}^2 \mu_{12}^2 e^{-i(\omega_1 - \omega_0)t_1 - t_1/T_2} \right|^2 \propto \mu_{01}^4 \mu_{12}^4 e^{-2t_1/T_2}. \quad (10)$$

The time-integrated response of the detector over t_3 is not detailed here. Note that, without contributions from the cross term, frequency-dependent terms that result in AC Stark hyperbolic side bands are eliminated by the square modulus. Furthermore, in this homodyne geometry, the measured decay equals the excited state lifetime as $T_1 = T_2/2$.

The above treatment applies for the emission of a single wave-mixing pathway. However, because of the broad bandwidths of the pulses employed in these experiments, the time evolution of individual emission signals reflects the contributions of multiple different wave-mixing pathways.²¹ Pathways like those in Figs. 8(a) and 8(b) interfere, resulting in quantum beat oscillations, and should collectively dictate the decay of the emission feature. As demonstrated by the perturbative simulation shown in the [supplementary material](#), Note 3, significant contributions from multiple pathways with nondegenerate NIR photons, like pathway 1 in Fig. 8(b), effectively eliminate lifetime variations between wave-mixing signals emitting from different reporter states. However, the experimental wave-mixing spectrum does exhibit reporter-state dependent lifetime variations. The duration of the short-lived component visibly

increases with $(n^*)^3$ of the reporter state. Moreover, the measured lifetimes track those of the Rydberg states coupled to the reporter states by a NIR-degenerate pathway like pathway 2 in Fig. 8(b). Supported by the early-delay Fourier transform [Fig. 5(b)], these NIR-degenerate pathways appear to be systematically enhanced relative to other pathways for the entire manifold of autoionizing states, allowing for the preferential coupling of the reporter states to themselves. The enhancement of NIR-degenerate pathways therefore leads to reporter-state dependent variations in the delay-dependence of these wave-mixing signals.

While not yet fully characterized in this system, the enhancement of NIR-degenerate pathways may potentially be explained by effects that cannot be fully captured by a perturbative picture of wave mixing. In a perturbative picture for a fully resonant wave-mixing process, the interaction of each pulse with the medium is treated as the linear absorption or emission of a photon from an eigenstate of the atom. For the system studied here, the emission of a broadband (~ 0.5 eV) NIR photon projects the XUV-induced coherence onto dark states located below the IP. The simultaneous interaction of a second NIR photon generates resonance-enhanced wave-mixing signals that emit from all states within the bandwidth of the NIR pulse, including the autoionizing states above the first IP. However, features suggesting significant deviations from a perturbative wave-mixing regime can be identified in this system. Previous experiments on long-lived Rydberg and dressed states in atomic helium have demonstrated that phase gratings due to the nonresonant AC Stark effect are instrumental in the formation of wave-mixing signals in this experimental geometry, leading to delays in emergence of higher diffraction orders.²² As shown in Fig. 6(b), the six-wave mixing signal emitting at the energy of the ($^2P_{1/2}$)6d/8s autoionizing state in the second emission band is delayed by 1.8 ± 0.4 fs relative to the wave-mixing signal in the first emission band, indicating that a purely perturbative wave mixing picture cannot adequately capture all the features observed of this experiment.

In the previous literature, the AC-Stark effect has been implicated in nonperturbative wave-mixing regimes as well as in pathway enhancement^{34–37} and therefore may provide an attractive mechanism by which to explain the enhancement of NIR-degenerate pathways in this experiment. However, the development of theoretical models that provide a general understanding of the impact of nonperturbative effects on wave-mixing signals is currently an active area of research.^{36,38–41} As few nonperturbative treatments of multi-level systems are currently available, more work is necessary to clarify the role of the AC-Stark effect on the evolution of wave-mixing signals in a complex system like the one studied here. Regardless of the mechanism, this experiment suggests that the enhancement of desirable wave-mixing pathways can assist in the measurement of ultrafast lifetimes by, in essence, reducing the complexity of the wave-mixing experiments. Once fully characterized, the mechanism that allows for pathway enhancement, such as the AC-Stark effect, may ultimately be utilized as a tool to enhance or eliminate particular nonlinear processes, providing experimentalists with substantive control over signal evolution.

V. CONCLUSIONS

Utilizing a noncollinear geometry with a short train of sub-femtosecond XUV pulses and two few-cycle NIR pulses, we directly

probe the time-domain evolution of spatially isolated wave-mixing signals from autoionizing states that decay on a variety of different timescales. This work not only represents the first successful generation of isolated XUV wave-mixing signals from states that decay on these timescales but also demonstrates that wave-mixing experiments performed in a noncollinear geometry may confer significant advantages over transient absorption experiments when measuring ultrafast decays. Due to the suppression of AC Stark energy level shifting and sidebands in homodyne wave-mixing experiments without the high harmonic XUV field, lifetimes of the short-lived ($^2P_{1/2}$)nd autoionizing states can be extracted directly from the time-domain signal despite persistent quantum beat oscillations. The observed lifetime trend can be attributed to wave-mixing pathways coupling the reporter states to themselves that dominate at the early delays. While the origins of this pathway enhancement are not yet fully established, delays between the emergence of four and six-wave mixing emission signals due to the accumulation of an AC-Stark grating provide evidence that nonperturbative effects impact signal generation and may influence signal evolution in this system. This work suggests that the selection of desired pathways, either through pathway enhancement as shown here or via multidimensional spectroscopic techniques, can support the measurement of ultrafast lifetimes, revealing dynamics that would have otherwise been obscured by the multiplexed nonlinear response of the system.

SUPPLEMENTARY MATERIAL

See the [supplementary material](#) for CMOS camera images for pulse overlap determination, a transient absorption spectrum of the ($^2P_{1/2}$)ns/d states over nearly a picosecond of delays, and a fully resonant, perturbative simulation of the wave-mixing spectrum.

ACKNOWLEDGMENTS

This work was supported by the Director, Office of Science, Office of Basic Energy Sciences through the Atomic, Molecular, and Optical Sciences Program of the Division of Chemical Sciences, Geosciences, and Biosciences of the U.S. Department of Energy at LBNL under Contract No. DE-AC02-05CH11231. A.P.F. acknowledges funding from the National Science Foundation Graduate Research Fellowship Program. We thank Luca Argenti and Robert Lucchese for helpful discussions.

REFERENCES

- ¹F. Krausz and M. Ivanov, *Rev. Mod. Phys.* **81**, 163 (2009).
- ²A. R. Beck, D. M. Neumark, and S. R. Leone, *Chem. Phys. Lett.* **624**, 119 (2015).
- ³K. Ramasesha, S. R. Leone, and D. M. Neumark, *Annu. Rev. Phys. Chem.* **67**, 41 (2016).
- ⁴B. Bernhardt, A. R. Beck, X. Li, E. R. Warrick, M. J. Bell, D. J. Haxton, C. W. McCurdy, D. M. Neumark, and S. R. Leone, *Phys. Rev. A* **89**, 023408 (2014).
- ⁵X. Li, B. Bernhardt, A. R. Beck, E. R. Warrick, A. N. Pfeiffer, M. Justine Bell, D. J. Haxton, C. W. McCurdy, D. M. Neumark, and S. R. Leone, *J. Phys. B: At., Mol. Opt. Phys.* **48**, 125601 (2015).
- ⁶M. Drescher, M. Hentschel, R. Kienberger, M. Uiberacker, V. Yakovlev, A. Scrinzi, T. Westerwalbesloh, U. Kleineberg, U. Heinzmann, and F. Krausz, *Nature* **419**, 803 (2002).

- ⁷F. Calegari, A. Trabattoni, A. Palacios, D. Ayuso, M. C. Castrovilli, J. B. Greenwood, P. Decleva, F. Martin, and M. Nisoli, *J. Phys. B: At., Mol. Opt. Phys.* **49**, 142001 (2016).
- ⁸S. Mukamel, *Principles of Nonlinear Optical Spectroscopy* (Oxford University Press, New York, 1995).
- ⁹P. Hamm and M. T. Zanni, *Concepts and Methods of 2D Infrared Spectroscopy* (Cambridge University Press, Cambridge, 2011).
- ¹⁰T. R. Calhoun, N. S. Ginsberg, G. S. Schlau-Cohen, Y. C. Cheng, M. Ballottari, R. Bassi, and G. R. Fleming, *J. Phys. Chem. B* **113**, 16291 (2009).
- ¹¹G. S. Schlau-Cohen, T. R. Calhoun, N. S. Ginsberg, E. L. Read, M. Ballottari, R. Bassi, R. van Grondelle, and G. R. Fleming, *J. Phys. Chem. B* **113**, 15352 (2009).
- ¹²D. Zigmantas, E. L. Read, T. Mancal, T. Brixner, A. T. Gardiner, R. J. Cogdell, and G. R. Fleming, *Proc. Natl. Acad. Sci. U. S. A.* **103**, 12672 (2006).
- ¹³Y. R. Shen, *Nature* **337**, 519 (1989).
- ¹⁴P. E. Ohno, S. A. Saslow, H. F. Wang, F. M. Geiger, and K. B. Eisenthal, *Nat. Commun.* **7**, 13587 (2016).
- ¹⁵C. L. Evans and X. S. Xie, *Annu. Rev. Anal. Chem.* **1**, 883 (2008).
- ¹⁶A. Zumbusch, G. R. Holtom, and X. S. Xie, *Phys. Rev. Lett.* **82**, 4142 (1999).
- ¹⁷W. Cao, E. R. Warrick, A. Fidler, S. R. Leone, and D. M. Neumark, *Phys. Rev. A* **94**, 021802 (2016).
- ¹⁸W. Cao, E. R. Warrick, A. Fidler, D. M. Neumark, and S. R. Leone, *Phys. Rev. A* **94**, 053846 (2016).
- ¹⁹W. Cao, E. R. Warrick, A. Fidler, S. R. Leone, and D. M. Neumark, *Phys. Rev. A* **97**, 023401 (2018).
- ²⁰E. R. Warrick, A. Fidler, W. Cao, E. Bloch, D. M. Neumark, and S. R. Leone, *Faraday Discuss.* **212**, 157 (2018).
- ²¹H. J. B. Marroux, A. P. Fidler, D. M. Neumark, and S. R. Leone, *Sci. Adv.* **4**, eaau3783 (2018).
- ²²A. P. Fidler, S. J. Camp, E. R. Warrick, E. Bloch, H. J. B. Marroux, D. M. Neumark, K. J. Schafer, M. B. Gaarde, and S. R. Leone, *Nat. Commun.* **10**, 1384 (2019).
- ²³H. Timmers, Y. Kobayashi, K. F. Chang, M. Reduzzi, D. M. Neumark, and S. R. Leone, *Opt. Lett.* **42**, 811 (2017).
- ²⁴S. Bengtsson, E. W. Larsen, D. Kroon, S. Camp, M. Miranda, C. L. Arnold, A. L'Huillier, K. J. Schafer, M. B. Gaarde, L. Rippe, and J. Mauritsson, *Nat. Photonics* **11**, 252 (2017).
- ²⁵W. Cao, E. R. Warrick, D. M. Neumark, and S. R. Leone, *New J. Phys.* **18**, 013041 (2016).
- ²⁶M. Wu, S. Chen, S. Camp, K. J. Schafer, and M. B. Gaarde, *J. Phys. B: At., Mol. Opt. Phys.* **49**, 062003 (2016).
- ²⁷A. Blouin, M.-M. Denariez Roberge, and P. Galarneau, *J. Opt. Soc. Am. B* **8**, 578 (1991).
- ²⁸E. J. Brown, Q. Zhang, and M. Dantus, *J. Chem. Phys.* **110**, 5772 (1999).
- ²⁹K. Maeda, K. Ueda, and K. Ito, *J. Phys. B: At., Mol. Opt. Phys.* **26**, 1541 (1993).
- ³⁰W. R. Johnson, K. T. Cheng, K. N. Huang, and M. Le Dourneuf, *Phys. Rev. A* **22**, 989 (1980).
- ³¹U. Fano and J. W. Cooper, *Rev. Mod. Phys.* **40**, 441 (1968).
- ³²C. Ott, A. Kaldun, P. Raith, K. Meyer, M. Laux, J. Evers, C. H. Keitel, C. H. Greene, and T. Pfeifer, *Science* **340**, 716 (2013).
- ³³S. Chen, M. Wu, M. B. Gaarde, and K. J. Schafer, *Phys. Rev. A* **88**, 033409 (2013).
- ³⁴A. M. Levine, N. Chencinski, W. M. Schreiber, A. N. Weizmann, and Y. Prior, *Phys. Rev. A* **35**, 2550 (1987).
- ³⁵W. Chalupczak, W. Gawlik, and J. Zachorowski, *Phys. Rev. A* **49**, 4895 (1994).
- ³⁶D. A. Coppeta, P. L. Kelley, P. J. Harshman, and T. K. Gustafson, *Phys. Rev. A* **53**, 925 (1996).
- ³⁷C.-Y. Tai, R. T. Deck, and C. Kim, *Phys. Rev. A* **37**, 163 (1988).
- ³⁸L. Chen, E. Palacino-González, M. F. Gelin, and W. Domcke, *J. Chem. Phys.* **147**, 234104 (2017).
- ³⁹M. F. Gelin, D. Egorova, and W. Domcke, *J. Phys. Chem. B* **115**, 5648 (2011).
- ⁴⁰V. V. Strelkov, *Phys. Rev. A* **93**, 053812 (2016).
- ⁴¹J. M. Shacklette and S. T. Cundiff, *J. Opt. Soc. Am. B* **20**, 764 (2003).